Electronic Supplementary Material (ESI) for Chemical Science.
This journal is © The Royal Society of Chemistry 2024

Supporting information

Leveraging metal node-linker self-assembly to access functional anisotropy of zirconium-based MOF-on-MOF epitaxial heterostructure thin film

Suvendu Panda, Susmita Kundu, Pratibha Malik, Ritesh Haldar*

Tata Institute of Fundamental Research Hyderabad, Gopanpally, Hyderabad 500046, India

1. Characterization techniques

1.1. X-ray diffraction

The X-ray diffraction patterns of the thin films were recorded on a Rigaku XDS 2000 diffractometer using nickel-filtered Cu Kα radiation (λ = 1.5418 Å). Data was collected in the range of 5 to 20° at room temperature (voltage 40 kV, current 200 mA). Out-of-plane XRD was recorded in $2\theta/\theta$ (step size 0.01, scan rate 0.2°/s) geometry. In-plane XRD was recorded in $2\theta/\varphi$ geometry with grazing incident angle (ω) of 0.3° and step size of 0.01 with scan rate 0.1°/s.

1.2. Scanning electron microscopy (SEM)

Morphology and cross-section of the thin films were characterized using field emission scanning electron microscopy (FESEM), JEOL JSM-7200F instrument with a cold emission gun operating at 30 kV.

1.3. Infrared spectroscopy

Infrared reflection absorption spectroscopy (IRRAS) of the thin films and attenuated total reflection (ATR) absorption spectroscopy of the Zr node solution were done using the Bruker Vertex 70v instrument, with a spectral resolution of 2 cm^{-1}. All the IRRAS results were recorded in grazing incidence reflection mode at an angle of incidence 70° relative to the surface, under vacuum at room temperature. 1-

octadecanethiol self-assembled monolayer (SAM) functionalized Au was used for background measurements.

1.4. X-ray photoelectron spectroscopy

Elemental (Br) depth profiling (etching rate 5.75 nm/min) of the thin film was performed using X-ray photoelectron spectrometer (PHI versaProbe III) within an ultrahigh vacuum (1×10^{-9} bar) environment. This instrument was equipped with an Al*Kα* X-ray source and a monochromator. For ion sputtering, Argon gas was used at 2 kV, over a 2×2 mm^2 area at an angle of 45˚ to the surface normal. The atomic composition was determined based on photoelectron peak areas and the relative sensitivity factors provided in PHI's MultiPak processing software.

1.5. Ultraviolet-vis spectroscopy

The transmission spectra of the thin films were recorded using Cary 5000 spectrometer with a UMA unit from Agilent.

1.6 Atomic Force Microscopy

AFM measurements were carried out using Nanosurf instrument in static mode. Images were processed using Gwyddion software.

2. Experimental section

2.1. Chemicals and materials

Zirconium(IV) propoxide solution (70 wt% in 1-propanol, TCI), bdc (TCI), NH_2-bdc (TCI), Br_2-bdc (TCI), acetic acid (99.9%, SRL), *N,N'*-dimethylformamide (Sigma Aldrich), anhydrous methanol (Sigma Aldrich), DI water, anhydrous 1 and 2-propanol (Sigma Aldrich), 11-Mercapto-1-undecanol (Sigma), and $ZrCl_4\cdot8H_2O$ (TCI) were used without any further purification.

2.2. Synthesis of (Zr_6 (μ^3-O)$_4$(μ^3-OH)$_4$($OOCCH_3$)$_{12}$) metal cluster solution

Metal cluster solution was synthesized following an earlier reported method.[1] 71 μL of a 70% zirconium propoxide [$Zr(O^nPr)_4$] solution in 1-propanol (0.0519 g, 0.158 mmol), 7 ml of DMF, and 4 ml of acetic acid (4.196 g, 70 mmol) mixture solution was heated in a 25 ml round-bottom flask at 130 ˚C for 2 h. A noticeable change in

solution from colorless to yellow was observed. Then the solution was allowed to cool down to room temperature (~ 298 K).

2.3. Syntheses of UiO-66/UiO-66-NH_2/UiO-66-Br_2 thin films at room temperature

A precursor solution was prepared by mixing 50 µL of as-prepared metal cluster solution and 50 µL of 7.184 mM bdc solution (in DMF). A droplet (100 µL) of this precursor solution was mixed well and drop casted on a functionalized Si/SiO_2 (1 cm ×1 cm) substrate at ambient conditions (298 ± 3 K, 50-60% RH). After 2 h the substrate was washed thoroughly to remove any excess deposition. The same procedure was repeated one more time to achieve a homogenous surface covering. The UiO-66 thin film was dried under N_2 flow. For UiO-66-NH_2 and UiO-66-Br_2, a similar procedure was followed, except the linkers were NH_2-bdc and Br_2-bdc (TCI), respectively. All the above-mentioned films were grown on various substrates: MUD (11-Mercapto-1-undecanol) functionalized gold substrate, SiO_2-coated QCM sensors, and hydroxyl functionalized Quartz substrate.

2.4. Synthesis of $(UiO\text{-}66)_B$-$(UiO\text{-}66\text{-}NH_2)_T$ thin film at room temperature

To synthesize a heterolayer of UiO-66/UiO-66-NH_2 thin film, a freshly prepared UiO-66 thin film (thickness ~ 250 nm) was used as a substrate. On top of this prefabricated bottom layer a droplet (100 µL) of the precursor solution, consisting of 50 µL of a prepared metal cluster solution and 50 µL of a 14.36 mM bdc (dissolved in DMF)) was evenly deposited. After 2 h, the substrate was rinsed thoroughly with DMF to remove excess deposition. This procedure was repeated one more time, washed with DMF, and dried under N_2 flow to achieve a ~ 450 nm heterolayer structure c. All the other heterolayer structures $(UiO\text{-}66\text{-}NH_2)_B$-$(UiO\text{-}66)_T$, $(UiO\text{-}66\text{-}Br_2)_B$-$(UiO\text{-}66)_T$, $(UiO\text{-}66\text{-}Br_2)_B$-$(UiO\text{-}66\text{-}NH_2)_T$, $(UiO\text{-}66)_B$-$(UiO\text{-}66\text{-}Br_2)_T$, $(UiO\text{-}66\text{-}NH_2)_B$-$(UiO\text{-}66\text{-}Br_2)_T$ were prepared following similar methodology.

2.5. Synthesis of $(UiO\text{-}66)_B$-$(UiO\text{-}66\text{-}Br_2)_{T/solvo}$ at solvothermal condition

0.5 mmol $ZrCl_4$, 0.25 mmol 1,4-benzenedicarboxylate, and 5 mmol acetic acid were mixed well with 10 ml of N,N'-dimethylformamide to get a precursor solution. Subsequently, an ambient condition synthesized UiO-66 thin film on a Si/SiO_2

substrate was placed horizontally into a Teflon-lined stainless steel autoclave, followed by the addition of the precursor solution. The solvothermal reaction was carried out at 393 K for 12 h. After the solvothermal synthesis, the obtained film was immersed in DMF and rinsed with DMF several times to get a $(UiO\text{-}66)_B\text{-}(UiO\text{-}66\text{-}Br_2)_{T/solvo}$ heterolayer thin film (Figure S8c, thickness ~ 450 nm).

2.6. Synthesis of UiO-66-NH_2 thin film by vapour assisted conversion (VAC) method

A precursor solution was prepared by dissolving 2.9 mmol $ZrOCl_2$, 2.9 mmol bdc-NH_2, and 232 mmol acetic acid in 1 ml of DMF. This solution was used for further processing.

In a closed 100 ml glass bottle, a mixture of acetic acid (0.8 ml) and DMF (4.2 ml) was used as a vapour source. Inside the container, a precleaned Si/SiO_2 substrate (1cm×1cm) was placed on a Teflon groove. A droplet (100 μL) of the precursor solution was evenly deposited on the substrate. The sealed bottle was placed in an oven preheated to 100 ˚C. After 3 h, it was removed from the oven to cool down to room temperature. The substrate was removed from the vessel and rinsed with DMF before further characterizations (Figure S2).

Table S1: Various reported synthesis methods for Zr-based MOF thin films.

Zr-MOFs	Methods	Reaction conditions	References
UiO-66	Electrochemical deposition	Electrophoretic deposition of powder on FTO glass	[2]
NU-1000	Electrochemical deposition	Electrophoretic deposition of powder on FTO glass	[2]
UiO-66	Solvothermal	1 $ZrCl_4$: 1 bdc: 1 H_2O: 500 Acetic acid: 1500 DMF at 393 K for 24h	[3]
UiO-66	Atomic layer deposition	$ZrCl_4$ + bdc+ H_2O+Acetic acid heated at 519 K	[4]
UiO-66	Layer-by-layer (LPE growth)	($ZrCl_4$ + HCl +DMF)) + (bdc +DMF) at 70 ˚C	[5]
UiO-66-NH_2	Layer-by-layer (LPE growth)	[$Zr_6O_4(OH)_4(OMc)_{12}$]/methacrylic acid (McOH) and an bdc-NH_2/methacrylic acid at 343 K	[6]
UiO-66	Solvothermal	Solution shearing of UiO-66 particles	[7]
UiO-66	Microwave synthesis	$ZrCl_4$ + bdc +DMF at 393 K, 30 min	[8]
UiO-66	Layer-by-layer (LPE growth)	($ZrCl_4$ + HCl +DMF)) + (bdc +DMF) at 70 ˚C	[9]
UiO-66	Layer-by-layer (LPE growth)	[$Zr_6O_4(OH)_4(OMc)_{12}$]/methacrylic acid (McOH) and an bdc-NH_2/methacrylic acid at 343 K	[10]
UiO-66, UiO-67, UiO-68	Vapour assisted conversion	$ZrOCl_2$•$8H_2O$+ related dicarboxylic acid+ acetic acid +DMF) 2h,393 K (acetic acid+ DMF vapour)	[11]
PCN-222	Vapour assisted conversion	$ZrOCl_2$•$8H_2O$+ TCPP+ Benzoic acid +DMF) 2h, 393 K (acetic acid+ DMF vapour)	[12]
UiO-66	Electrochemical deposition	Zirconium foil & bdc:HNO_3:H_2O:AA:DMF =	[13]

		1:2:4:5/10/50:130	
NU-901	Solvothermal	$ZrCl_4$ + benzoic acid + H_4TBAPy+ 120 ˚C+24 h	[14]
NU-1000	Solvothermal	$ZrOCl_2 \cdot 8H_2O$ + H_4TBAPy+DMF+Benzoic acid + TFA + 120 ˚C+24 h	[14]
UiO-66	Solution shearing	(Zr(O*n*Pr)$_4$ and bdc) , DMSO, DMF, 100 to 160 ˚C	[15]
UiO-66	Epitaxial growth by spin coating	UiO-66 seed solution coting on AAO membrane at RT	[16]
UiO-66	Solvothermal	($ZrCl_4$ + ACOH +DMF+ water + 1,4-BDC at 150 ˚C, 6 h	[17]
UiO-66	Layer-by-layer	$ZrCl_4$+ACOH+DI water +DMF, 393 K,12h = Metal cluster Metal cluster + bdc, 298 K,12 h	[18]

Table S2: Reaction conditions for UiO-66 thin film growth at room temperature.

(Concentration of metal node solution was determined based on the assumption of complete conversion during the metal node synthesis reaction)

	Exp.	**Precursor solution**		**Droplet volume (μL)**	**Substrate**	**Reaction time (h)**
		Metal node ($Zr_6O_8(OOCCH_3)_{12}$) (in 50 μL DMF)	bdc (in 50 μL DMF)			
Variation of precursor concentration and reaction time	1	0.188 μmol	0.718 μmol	50	Si/SiO_2	0.5
	2	0.188 μmol	0.718 μmol	50	Si/SiO_2	2
	3	0.188 μmol	0.718 μmol	50	Si/SiO_2	3.5
	4	0.188 μmol	0.718 μmol	50	Si/SiO_2	5
	5	0.188 μmol	0.718 μmol	50	Si/SiO_2	0.5
	6	0.188 μmol	0.359 μmol	50	Si/SiO_2	2
	7	0.188 μmol	0.359 μmol	50	Si/SiO_2	3.5
	8	0.188 μmol	0.359 μmol	50	Si/SiO_2	5
Variation of droplet volume and reaction time	9	0.188 μmol	0.359 μmol	100	Si/SiO_2	0.5
	10	0.188 μmol	0.359 μmol	100	Si/SiO_2	2
	11	0.188 μmol	0.359 μmol	100	Si/SiO_2	3.5
	12	0.188 μmol	0.359 μmol	100	Si/SiO_2	5
	13	0.188 μmol	0.359 μmol	100	Si/SiO_2	2+2
Variation of substrate	14	0.188 μmol	0.359 μmol	100	MUD-Au	2+2
	15	0.188 μmol	0.359 μmol	100	QCM sensor	2+2
	16	0.188 μmol	0.359 μmol	100	Quartz	2+2

Table S3: Reaction conditions for UiO-66-NH_2 thin film growth at room temperature.

	Exp.	**Precursor solution**		**Droplet volume (µL)**	**Substrate**	**Reaction time (h)**
		Metal node ($Zr_6O_8(OOCCH_3)_{12}$ (in 50 µL DMF)	**bdc-NH_2 (in 50µL DMF)**			
Variation of Droplet volume and reaction time	17	0.188 µmol	0.359 µmol	100	Si/SiO_2	0.5
	18	0.188 µmol	0.359 µmol	100	Si/SiO_2	2
	19	0.188 µmol	0.359 µmol	100	Si/SiO_2	3.5
	20	0.188 µmol	0.359 µmol	100	Si/SiO_2	5
	21	0.188 µmol	0.718 µmol	100	Si/SiO_2	0.5
	22	0.188 µmol	0.718 µmol	100	Si/SiO_2	2
	23	0.188 µmol	0.718 µmol	100	Si/SiO_2	3.5
	24	0.188 µmol	0.718 µmol	100	Si/SiO_2	5
	25	0.188 µmol	0.718 µmol	100	Si/SiO_2	2+2
Variation of substrate	26	0.188 µmol	0.718 µmol	100	MUD-Au	2+2
	27	0.188 µmol	0.718 µmol	100	QCM sensor	2+2
	28	0.188 µmol	0.718 µmol	100	Quartz	2+2

Table S4: Reaction conditions for UiO-66-Br_2 thin film growth at room temperature.

	Exp.	Precursor solution		Droplet volume (µL)	Substrate	Reaction time (h)
		Metal node ($Zr_6O_8(OOCCH_3)_{12}$ (in 50 µL DMF)	**bdc-Br_2 (in 50 µL DMF)**			
Variation of precursor concentration and reaction time	29	0.188 µmol	0.718 µmol	100	Si/SiO_2	0.5
	30	0.188 µmol	0.718 µmol	100	Si/SiO_2	2
	31	0.188 µmol	0.718 µmol	100	Si/SiO_2	3.5
	32	0.188 µmol	0.718 µmol	100	Si/SiO_2	5
	33	0.188 µmol	0.359 µmol	100	Si/SiO_2	0.5
	34	0.188 µmol	0.359 µmol	100	Si/SiO_2	2
	35	0.188 µmol	0.359 µmol	100	Si/SiO_2	3.5
	36	0.188 µmol	0.359 µmol	100	Si/SiO_2	5
	37	0.188 µmol	0.239 µmol	100	Si/SiO_2	0.5
	38	0.188 µmol	0.239 µmol	100	Si/SiO_2	2
	39	0.188 µmol	0.239 µmol	100	Si/SiO_2	3.5
	40	0.188 µmol	0.239 µmol	100	Si/SiO_2	5
	41	0.188 µmol	0.239 µmol	100	Si/SiO_2	2+2
Variation of substrate	42	0.188 µmol	0.239 µmol	100	MUD-Au	2+2
	43	0.188 µmol	0.239 µmol	100	QCM sensor	2+2
	44	0.188 µmol	0.239 µmol	100	Quartz	2+2

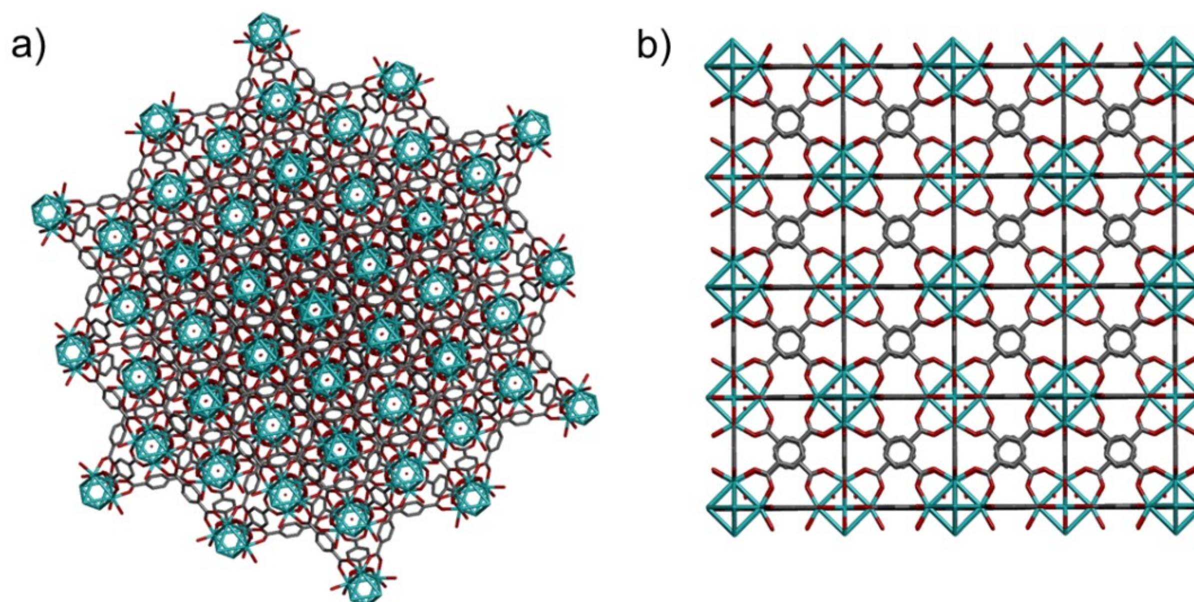

Figure S1. View of the UiO-66 structure along a) [111] and b) [200] orientations.

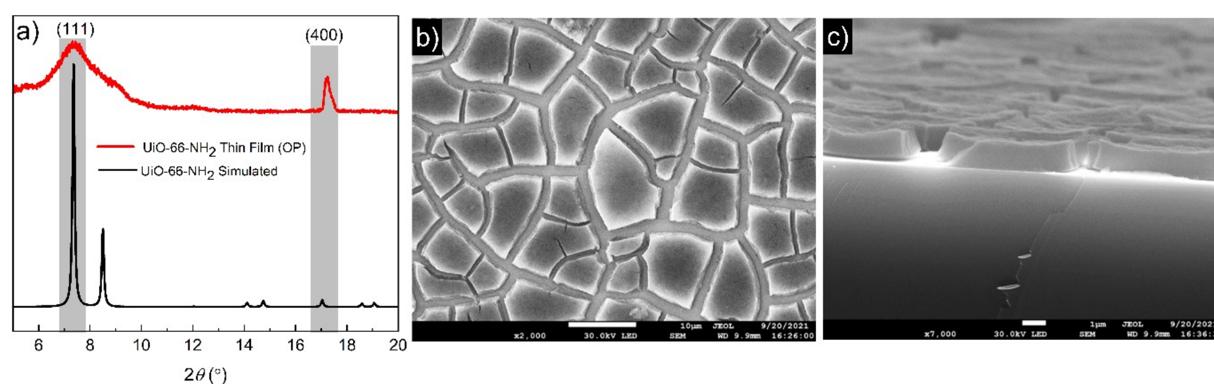

Figure S2. a) Out-of-plane XRD pattern of UiO-66-NH_2 thin film (red) obtained by VAC method and the simulated diffraction pattern (black); b) top-view and c) cross-section SEM micrograph of UiO-66-NH_2 film synthesized by VAC method.

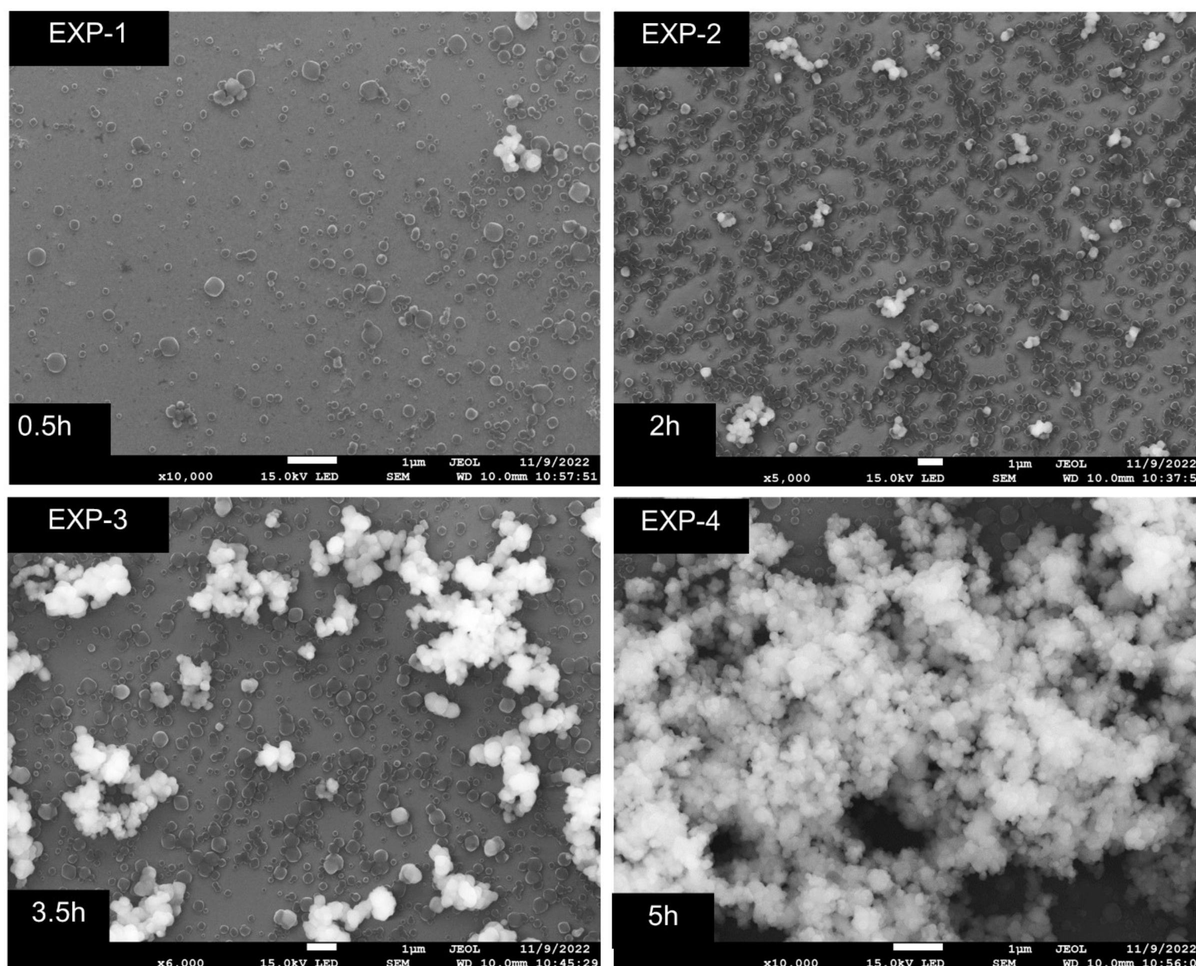

Figure S3. Top-view SEM images of UiO-66 thin films for EXP (1-4).

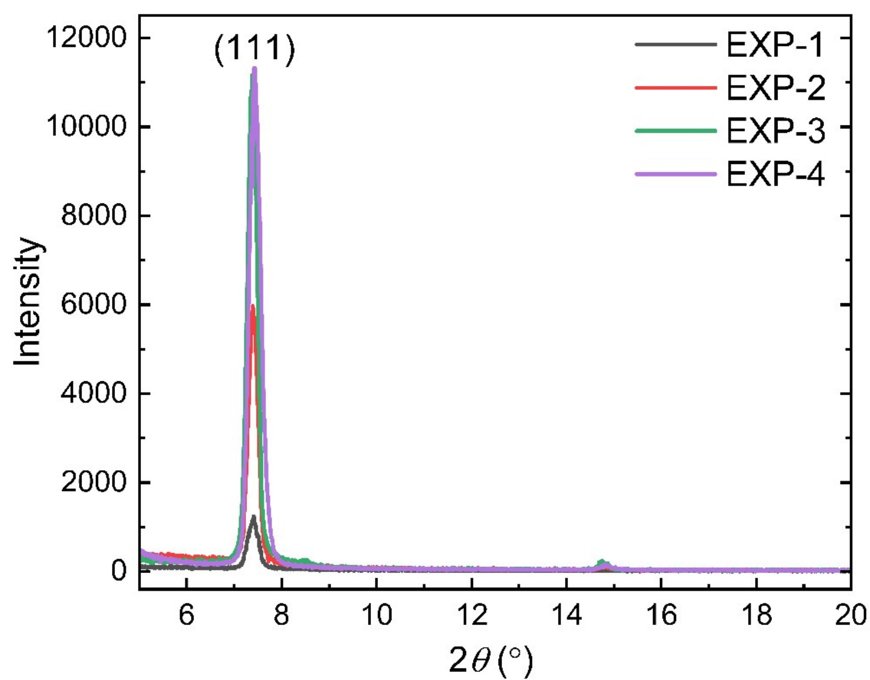

Figure S4. Out-of-plane X-ray diffraction patterns of UiO-66 thin films for EXP (1-4).

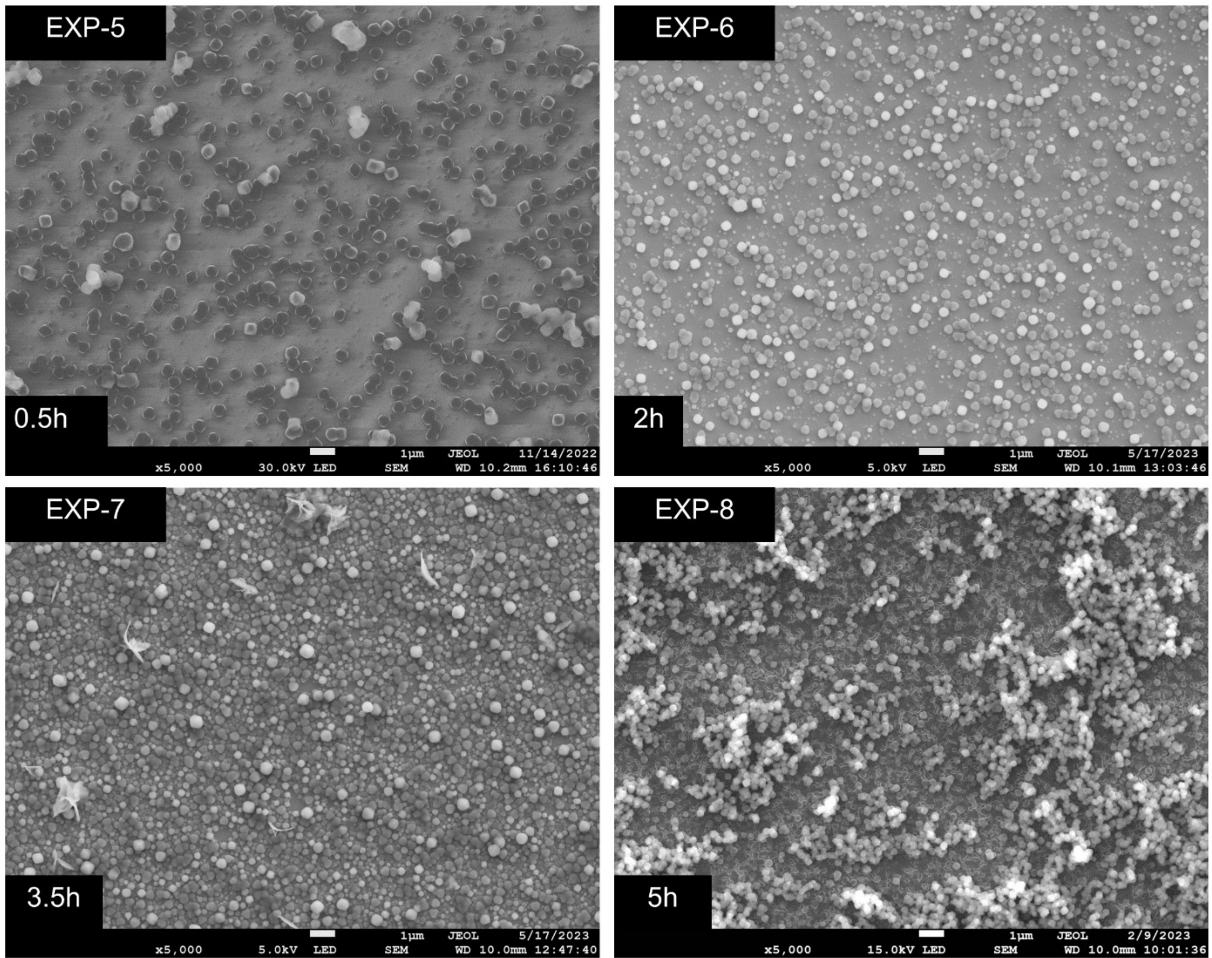

Figure S5. Top-view SEM images of UiO-66 thin films for EXP (5-8).

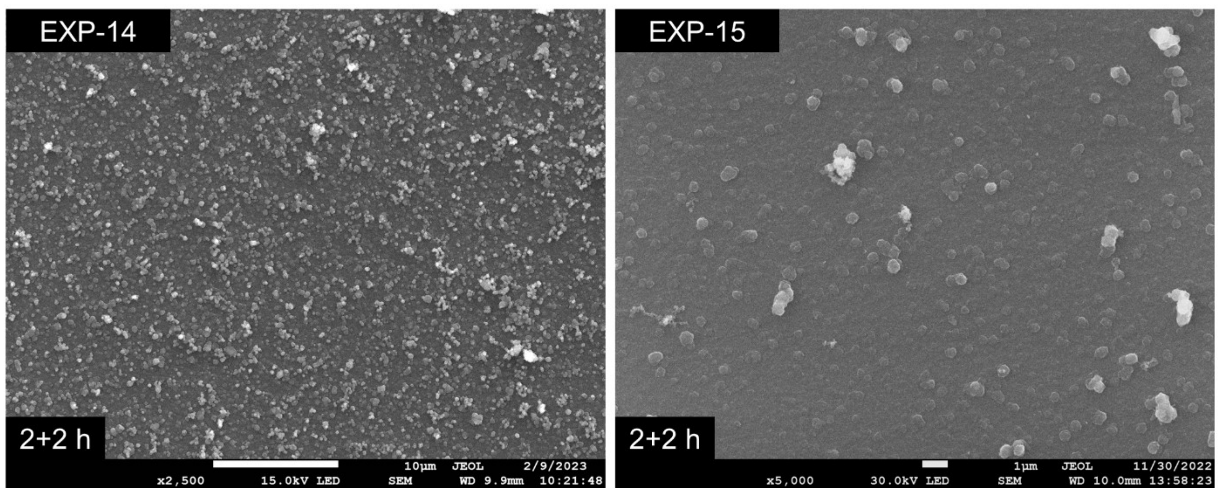

Figure S6. Top-view SEM images of UiO-66 thin films for EXP (14-15).

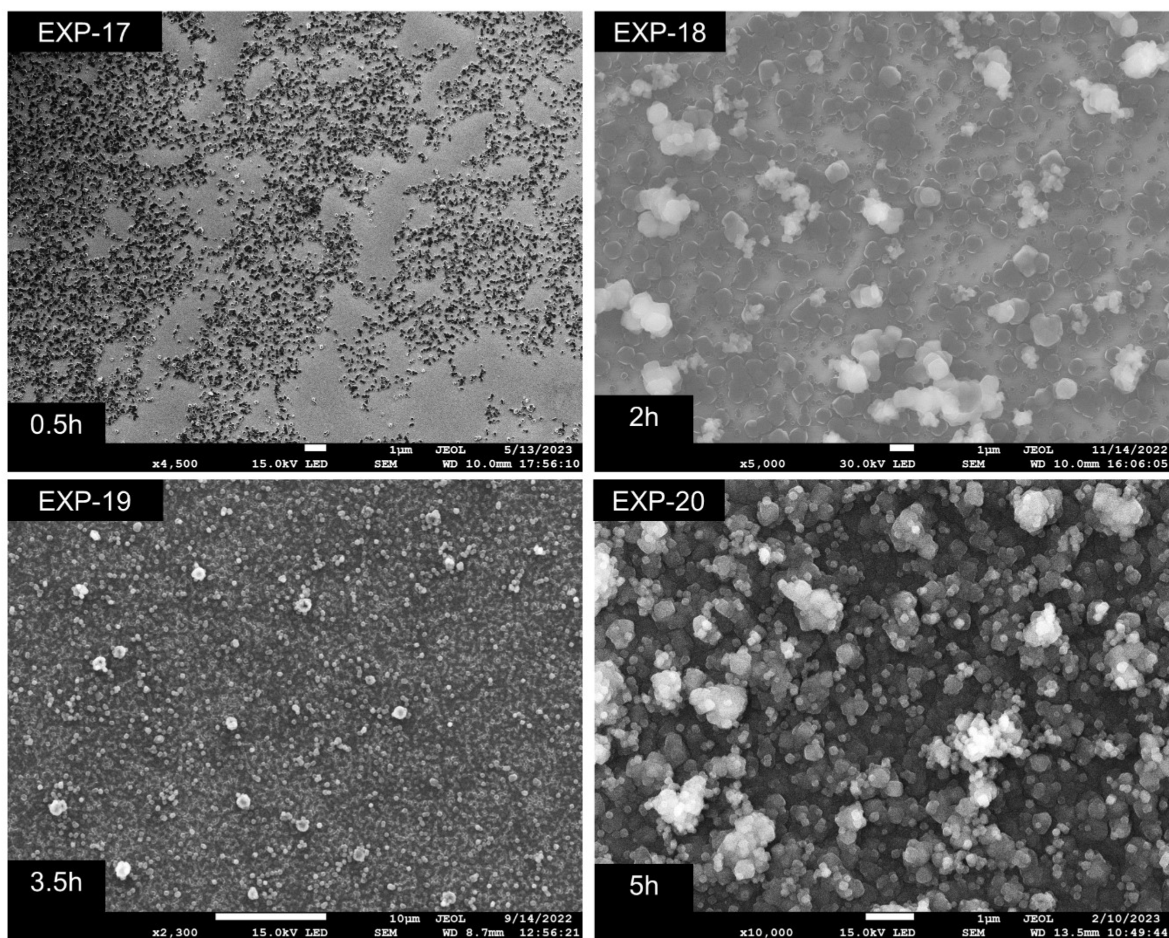

Figure S7. Top-view SEM images of UiO-66-NH_2 thin films for EXP (17-20).

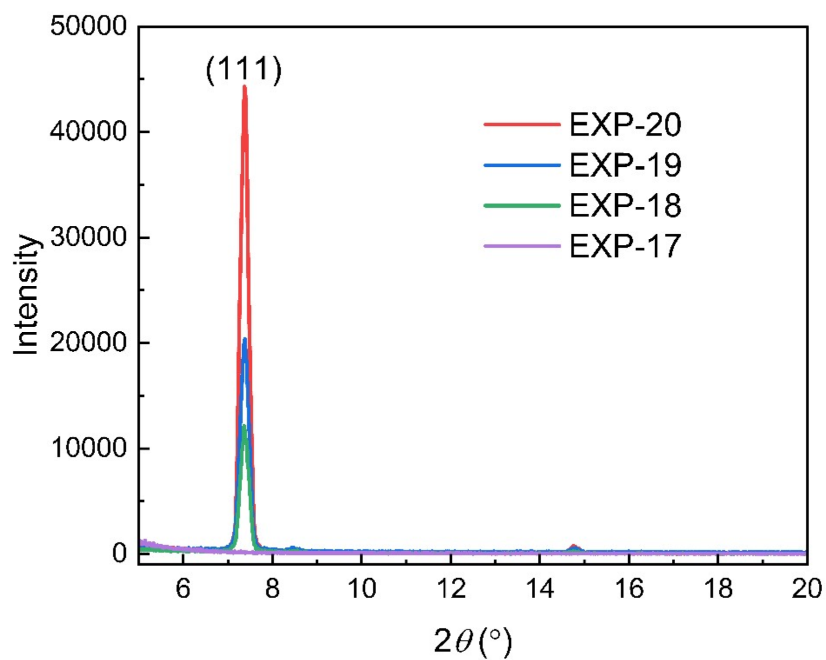

Figure S8. Out-of-plane X-ray diffraction patterns of UiO-66-NH_2 thin films for EXP (17-20).

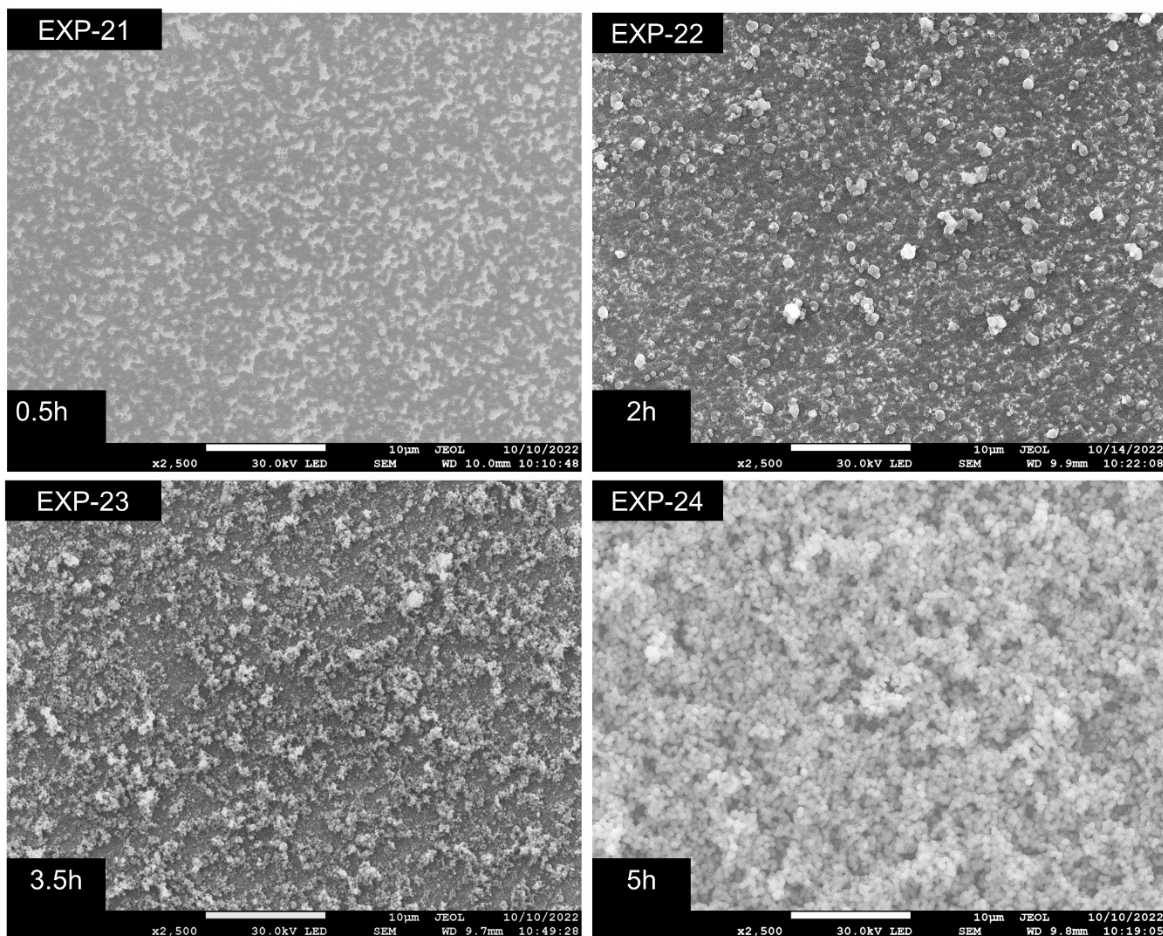

Figure S9. Top-view SEM images of UiO-66-NH_2 thin films for EXP (21-24).

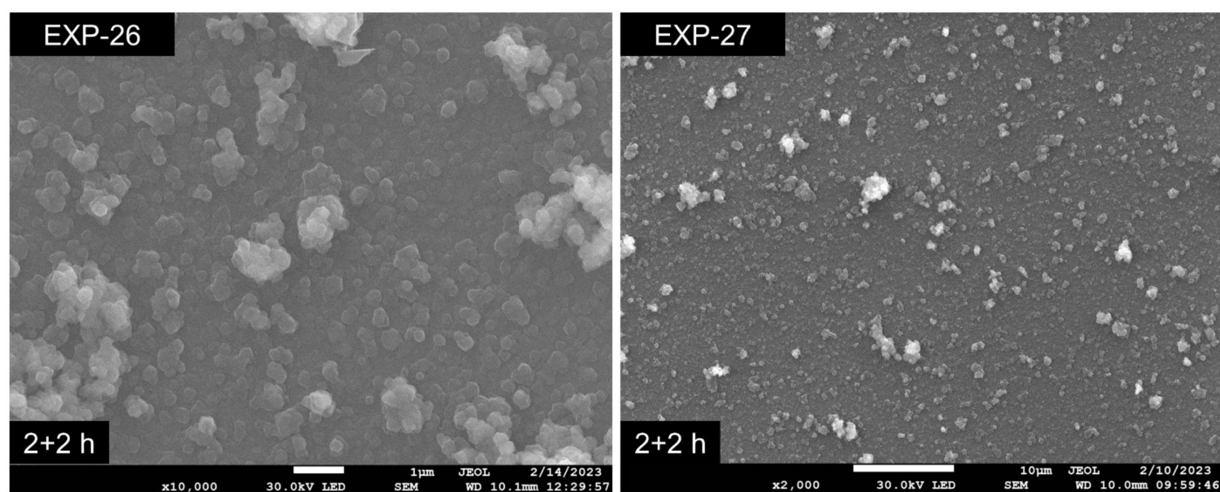

Figure S10. Top-view SEM images of UiO-66-NH_2 thin films for EXP (26-27).

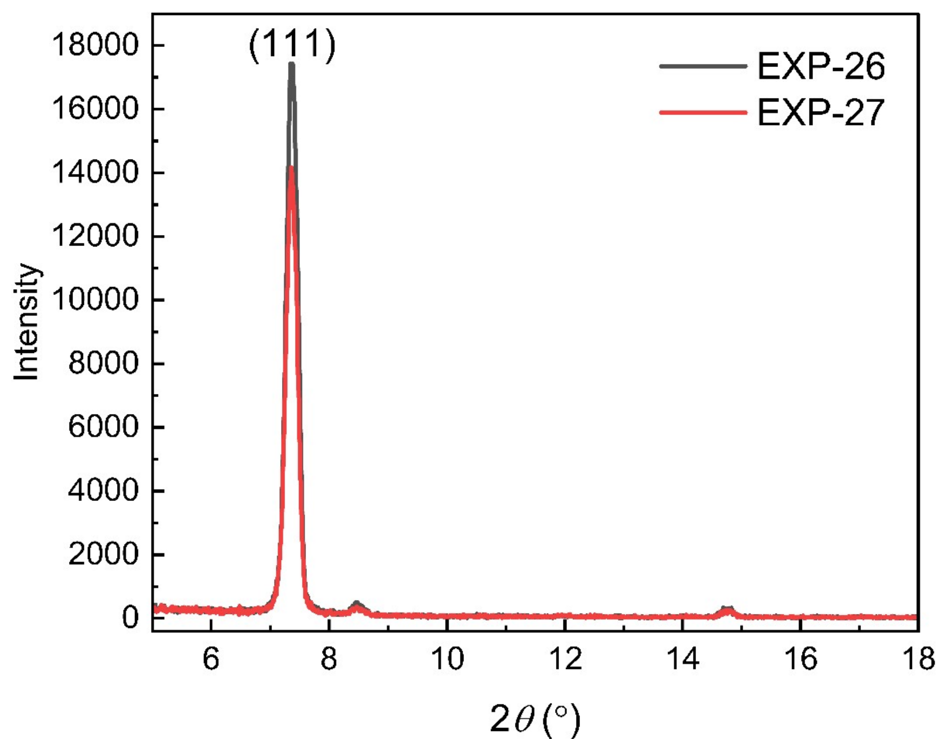

Figure S11. Out-of-plane X-ray diffraction patterns of UiO-66-NH_2 thin films for EXP (26-27).

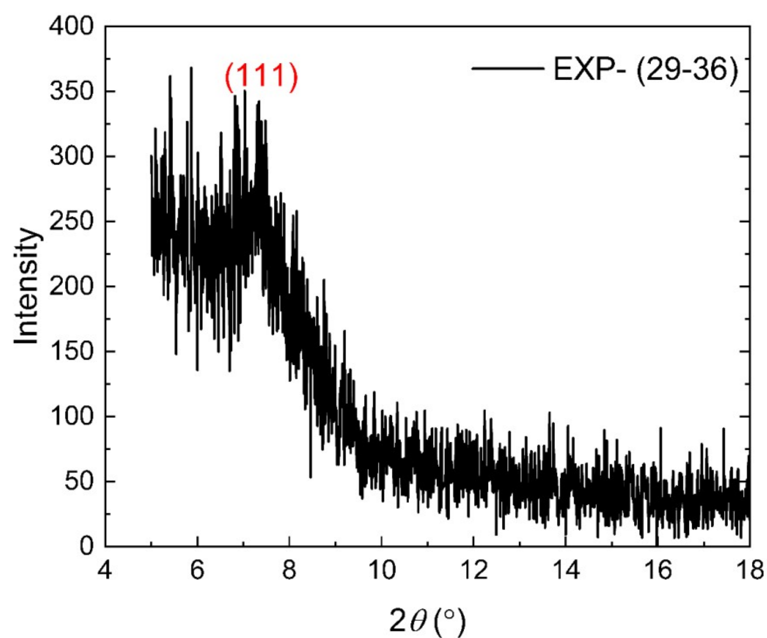

Figure S12. Out-of-plane X-ray diffraction patterns of UiO-66-Br_2 thin films for EXP (29-36).

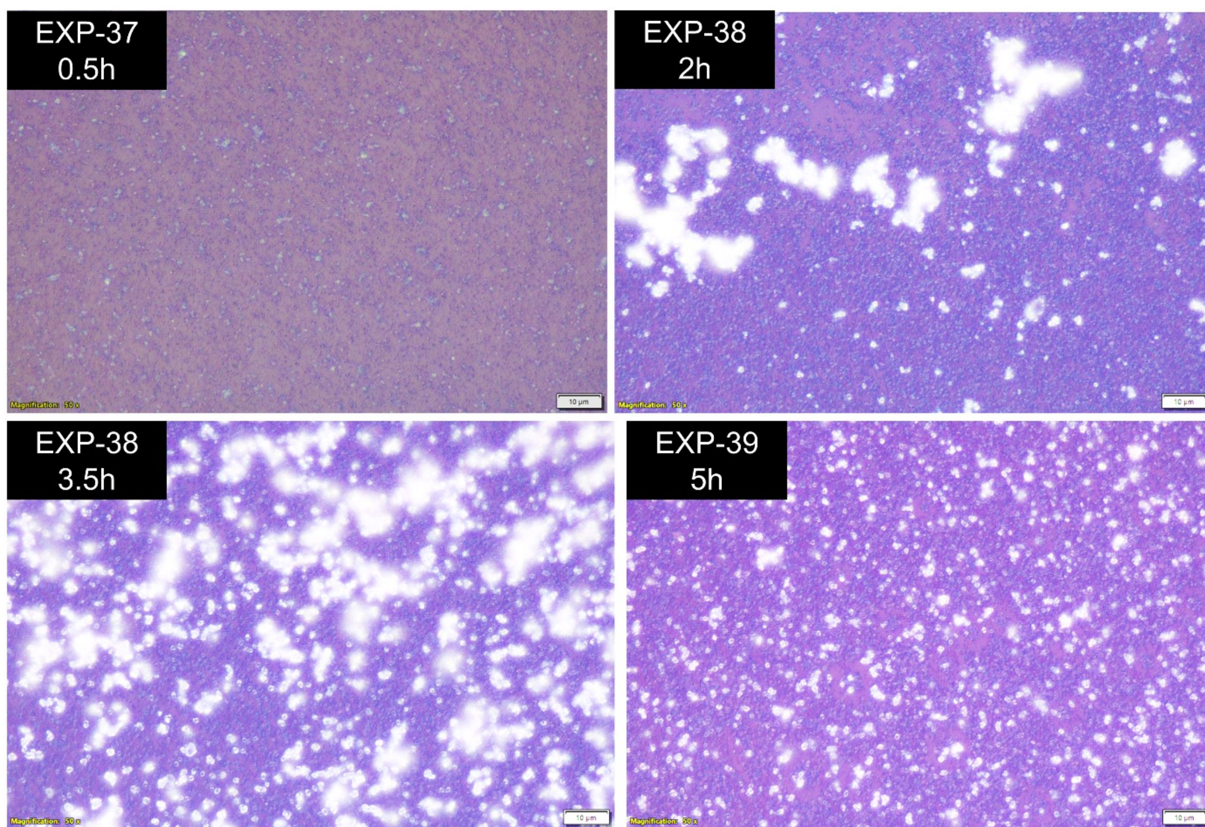

Figure S13. Optical microscope images of UiO-66-Br_2 thin films for EXP (37-39).

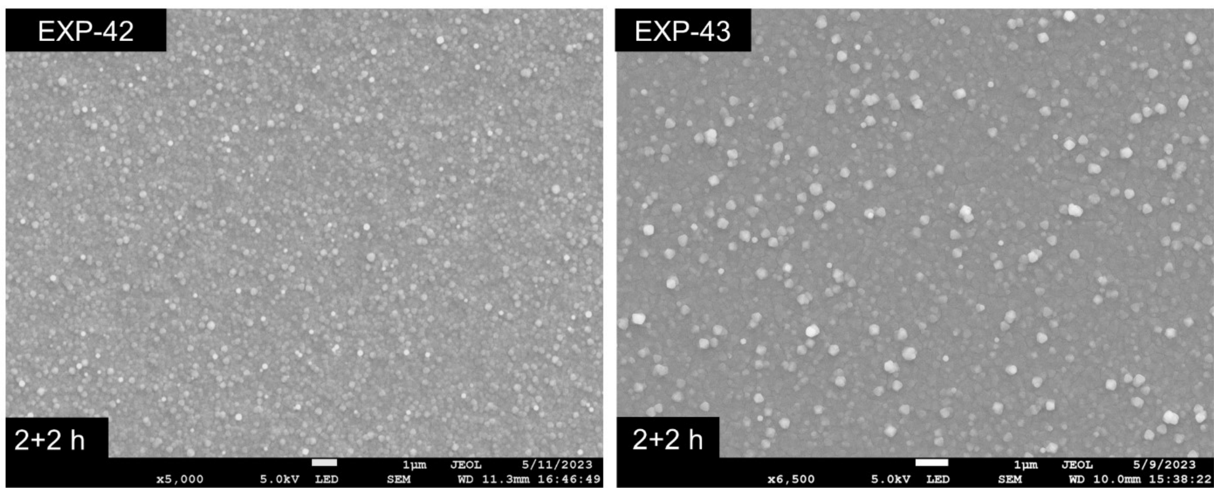

Figure S14. Top-view SEM images of UiO-66-Br_2 thin films for EXP (42-43).

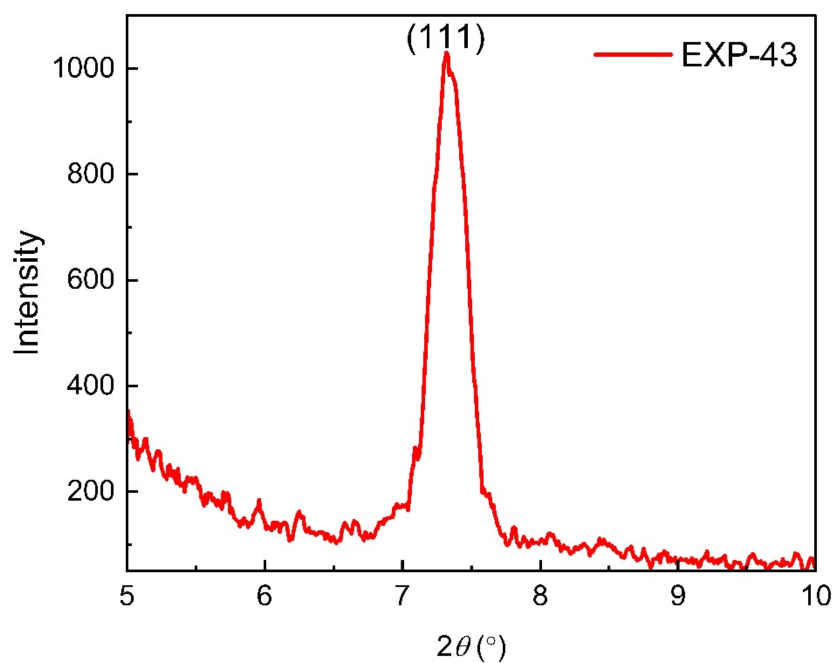

Figure S15. Out-of-plane X-ray diffraction pattern of UiO-66-Br_2 thin film for EXP- 43.

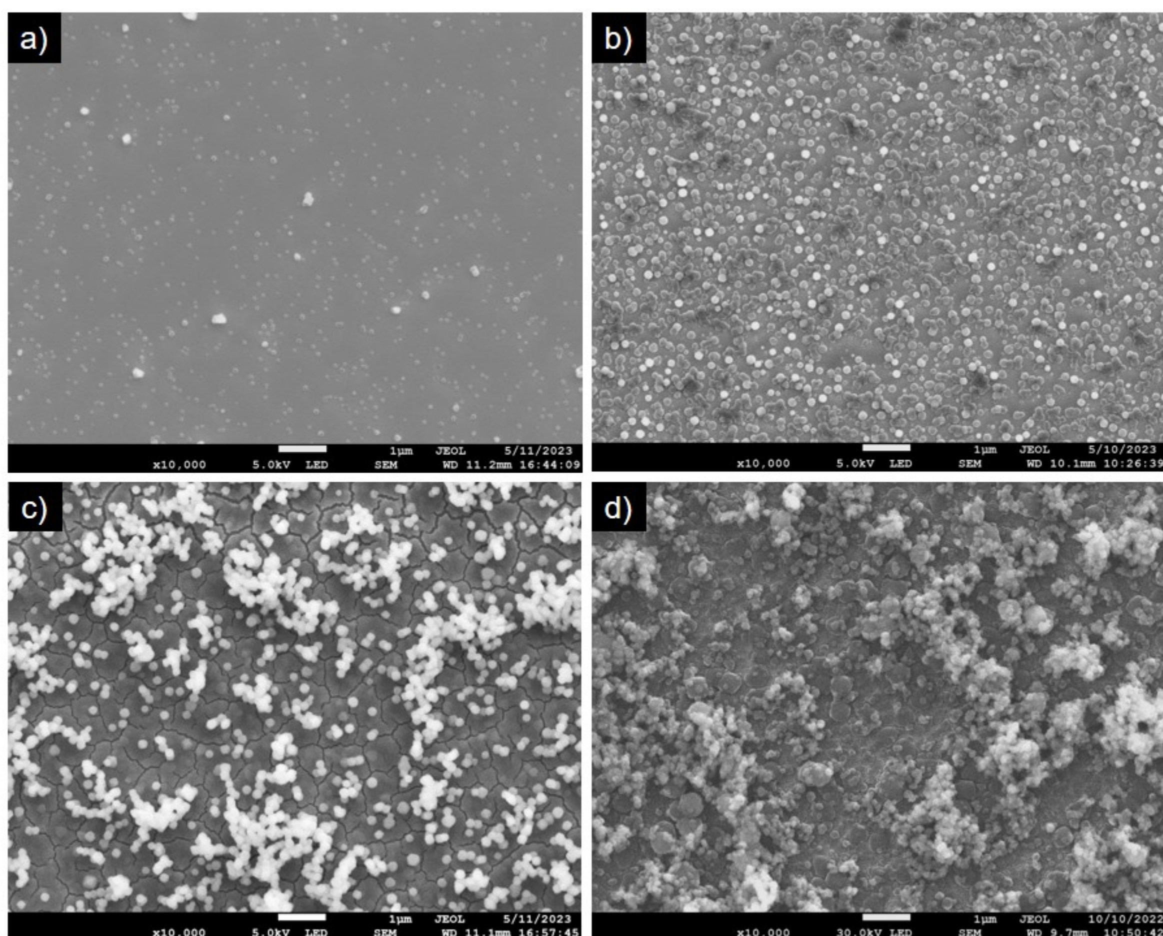

Figure S16. SEM images of the UiO-66 thin films at various deposition time; a) 0.5, b) 2, c) 3.5, and d) 5 h.

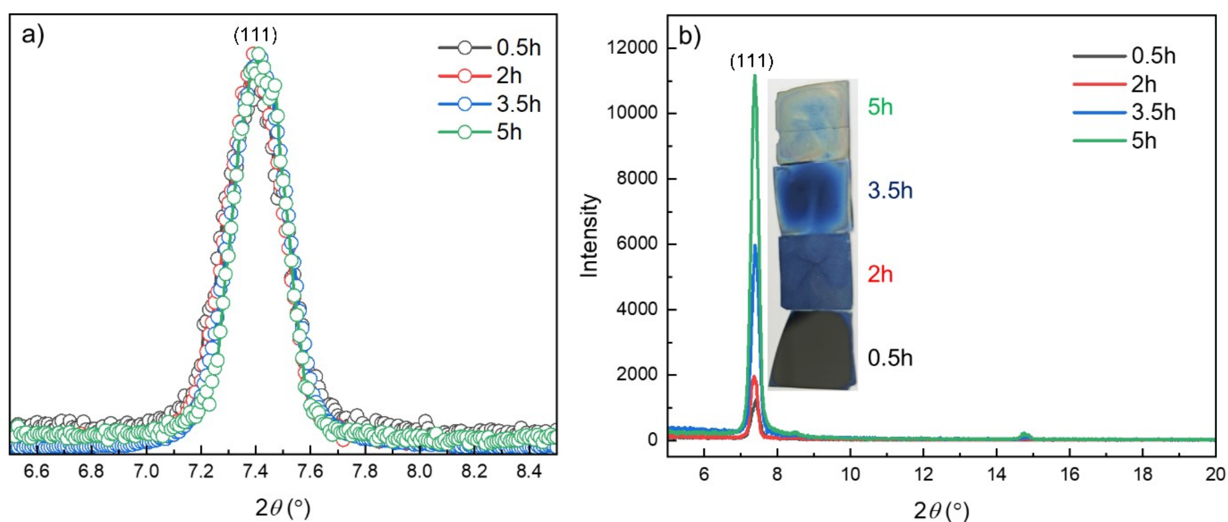

Figure S17. Out-of-plane XRD patterns of UiO-66 thin films obtained after different reaction time: a) normalized peak intensities for (111) plane showing similar FWHM, b) intensity enhancement for the peak corresponding to (111) plane, and the optical images of the thin films.

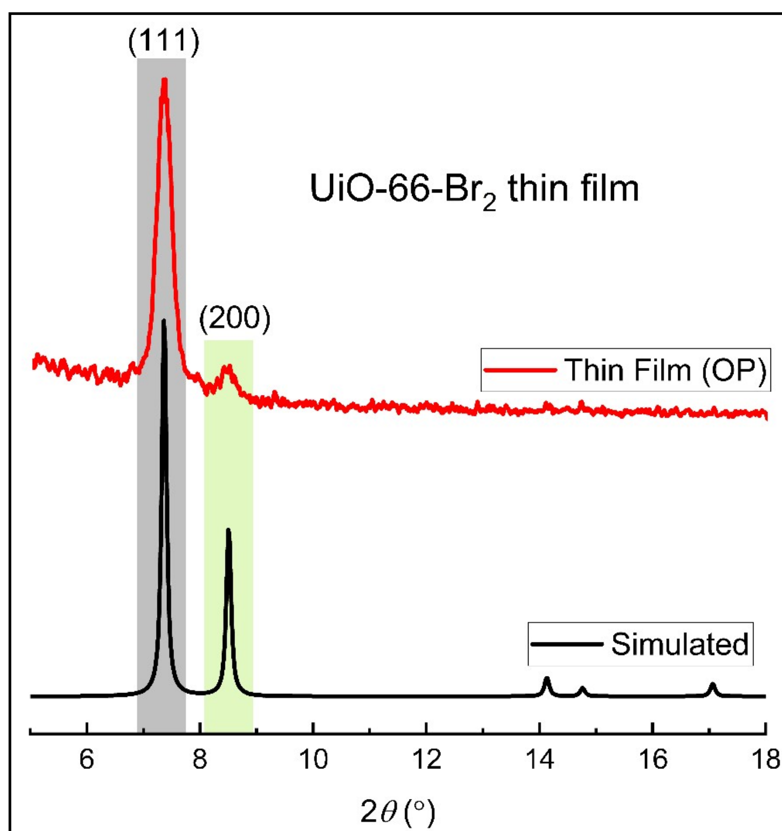

Figure S18. Out-of-plane XRD pattern of UiO-66-Br_2 thin film at ambient condition (red), and the simulated diffraction pattern (black).

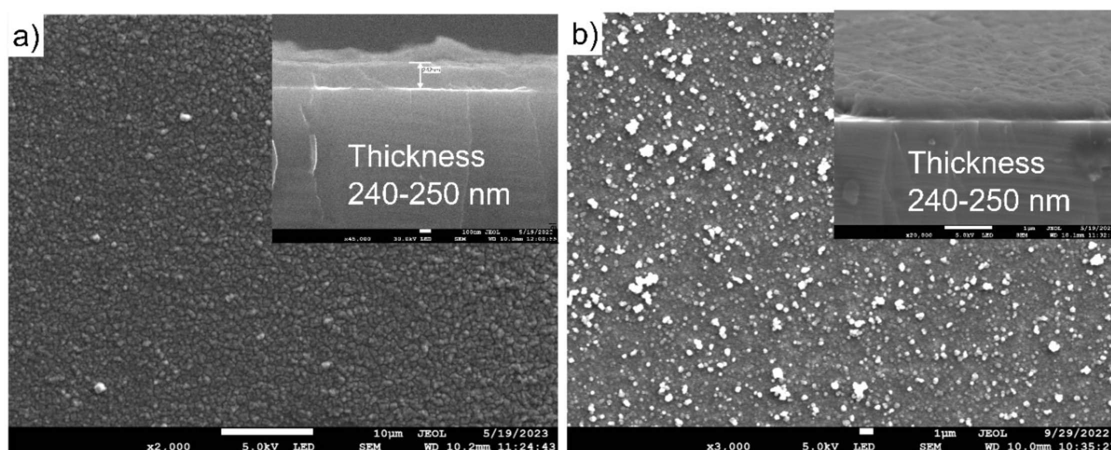

Figure S19. SEM micrographs of the a) UiO-66-NH_2 and b) UiO-66-Br_2 thin films, inset: respective cross-section images.

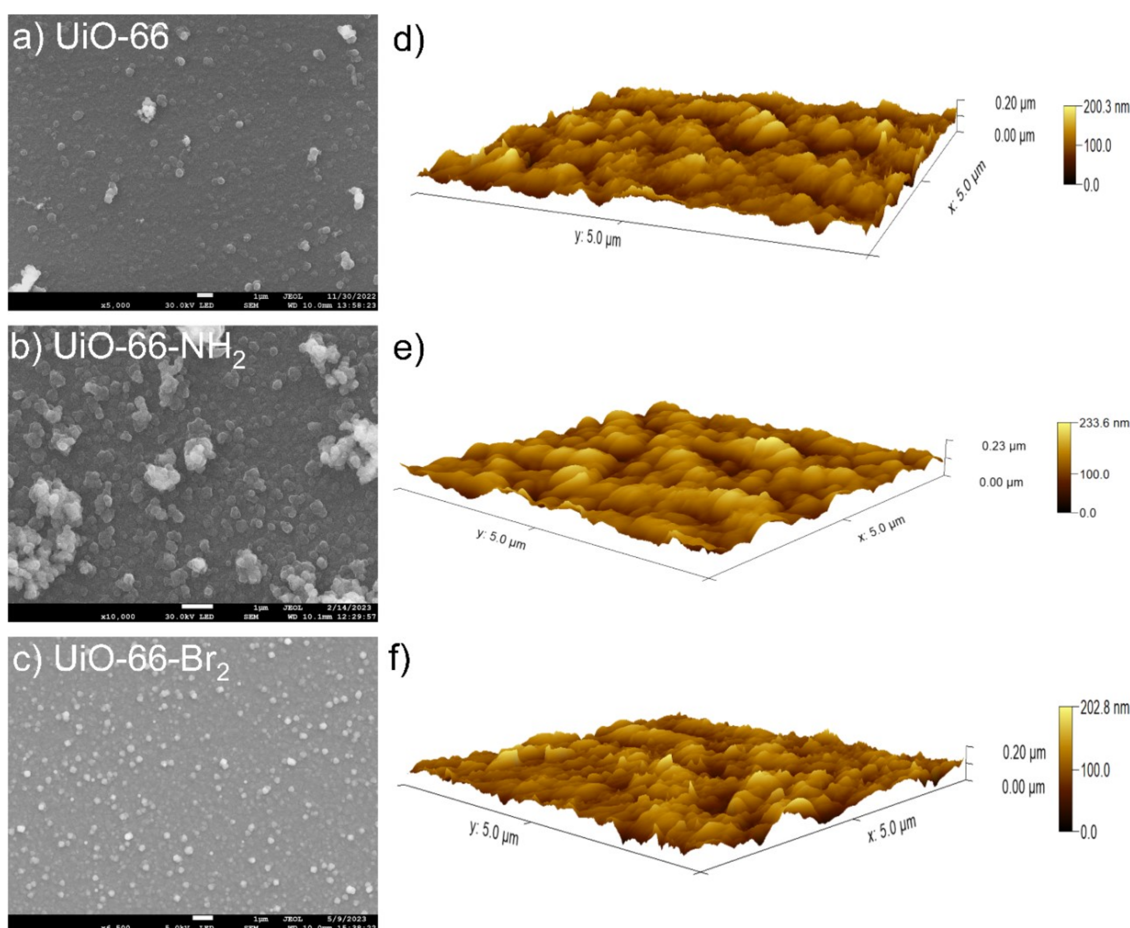

Figure S20. Top view SEM morphological images of the a) UiO-66, b) UiO-66-NH_2, and c) UiO-66-Br_2 thin films (scale bar = 1 µm). Atomic force microscopy (AFM images of d) UiO-66, e) UiO-66-NH_2, and f) UiO-66-Br_2 thin films.

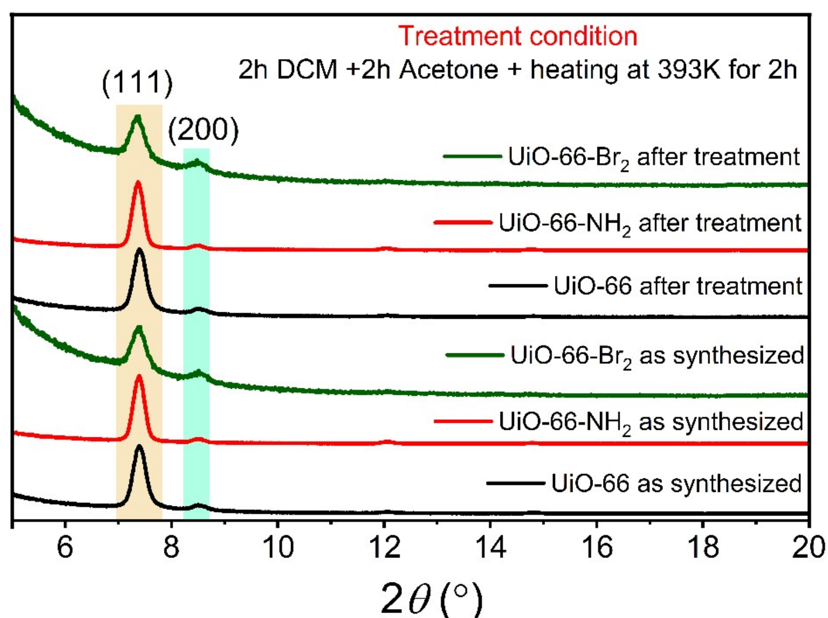

Figure S21. Out-of-plane XRD patterns of UiO-66 (black), UiO-66-NH_2 (red), and UiO-66-Br_2 (green) thin films (on functionalized Au substrate) before and after the treatment at thermal and chemical conditions.

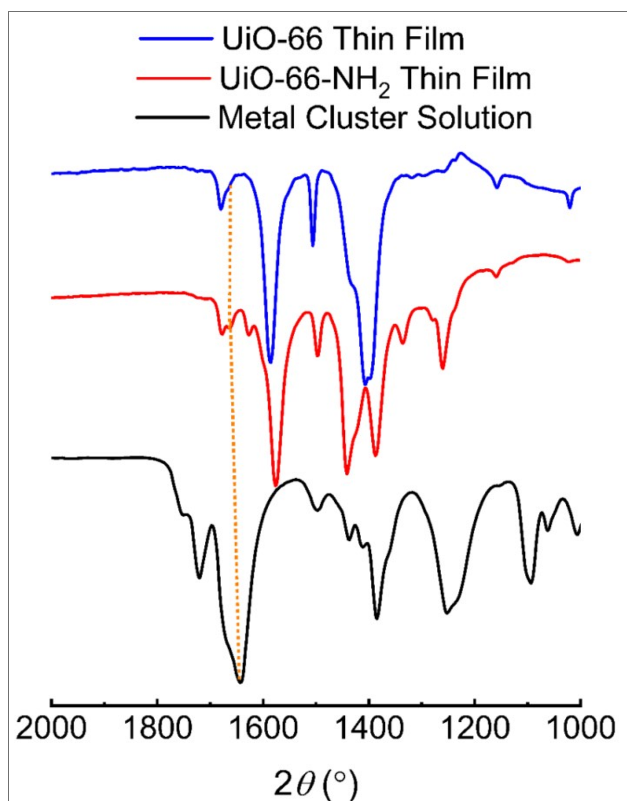

Figure S22. IRRAS of the UiO-66 thin film, UiO-66-NH_2 thin film and ATR IR of the metal node ($Zr_6(O)_4(OH)_4(OOCCH_3)_{12}$) solution, showing C=O stretching from the acetate.

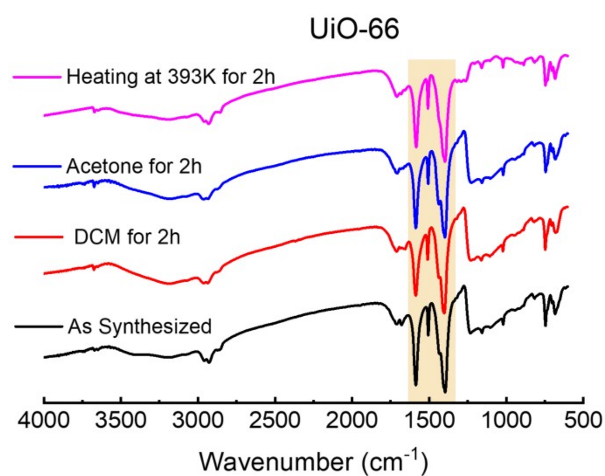

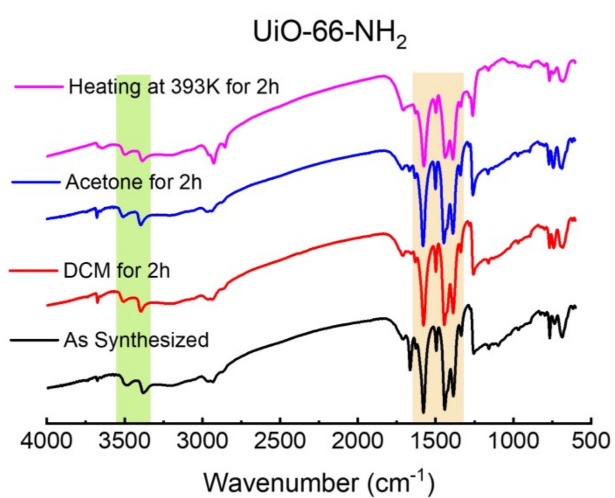

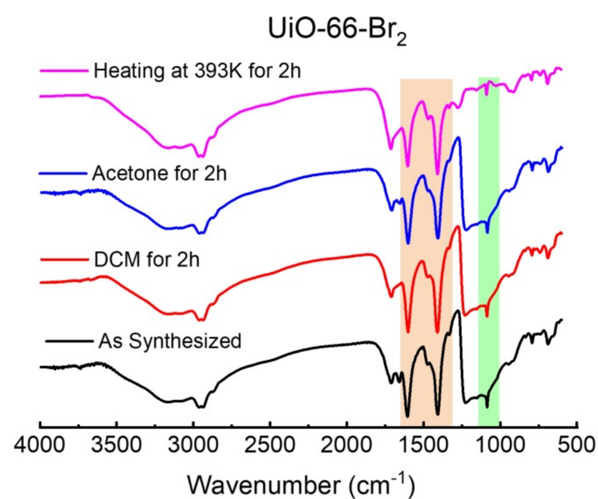

Figure S23. IRRAS of the UiO-66, UiO-66-NH_2, and UiO-66-Br_2 thin film before and after various solvent and thermal treatments.

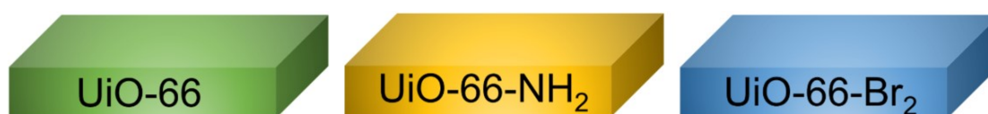

Figure S24. Top and cross-section (inset) SEM micrographs of heterolayers. a) UiO-66$_{(B)}$-UiO-66-NH$_{2(T)}$, b) UiO-66-NH$_2$ $_{(B)}$-UiO-66 $_{(T)}$, c) UiO-66$_{(B)}$-UiO-66-Br$_{2(T)/solvo}$, d) UiO-66-NH$_2$ $_{(B)}$-UiO-66.Br$_{2(T)}$, e) UiO-66-Br$_2$ $_{(B)}$-UiO-66$_{(T)}$, f) UiO-66-Br$_2$ $_{(B)}$-UiO-66-NH$_{2(T)}$

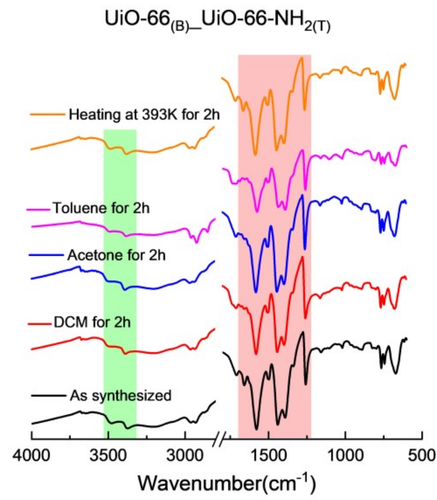

UiO-66(B)_UiO-66-NH2(T)
Heating at 393K for 2h
Toluene for 2h
Acetone for 2h
DCM for 2h
As synthesized
4000
3500
3000
1500
1000
500
Wavenumber(cm-1)

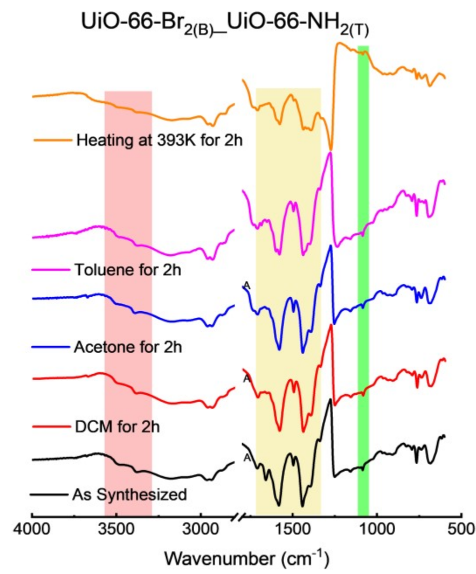

UiO-66-Br2(B)_UiO-66-NH2(T)
Heating at 393K for 2h
Toluene for 2h
Acetone for 2h
DCM for 2h
As Synthesized
4000
3500
3000
1500
1000
500
Wavenumber (cm-1)

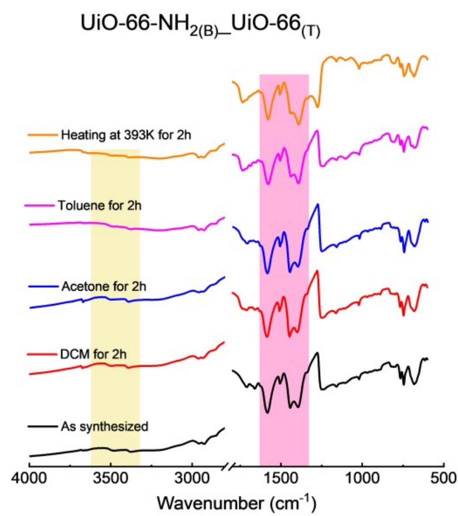

UiO-66-NH2(B)_UiO-66(T)
Heating at 393K for 2h
Toluene for 2h
Acetone for 2h
DCM for 2h
As synthesized
4000
3500
3000
1500
1000
500
Wavenumber (cm-1)

Figure S25. IRRAS analysis of heterolayers before and after various solvent and thermal treatment. UiO-$66_{(B)}$-UiO-66-$NH_{2(T)}$ (left), UiO-66-$NH_{2\ (B)}$-UiO-$66_{\ (T)}$ (middle), UiO-66-$Br_{2\ (B)}$-UiO-66-$NH_{2(T)}$ (right).

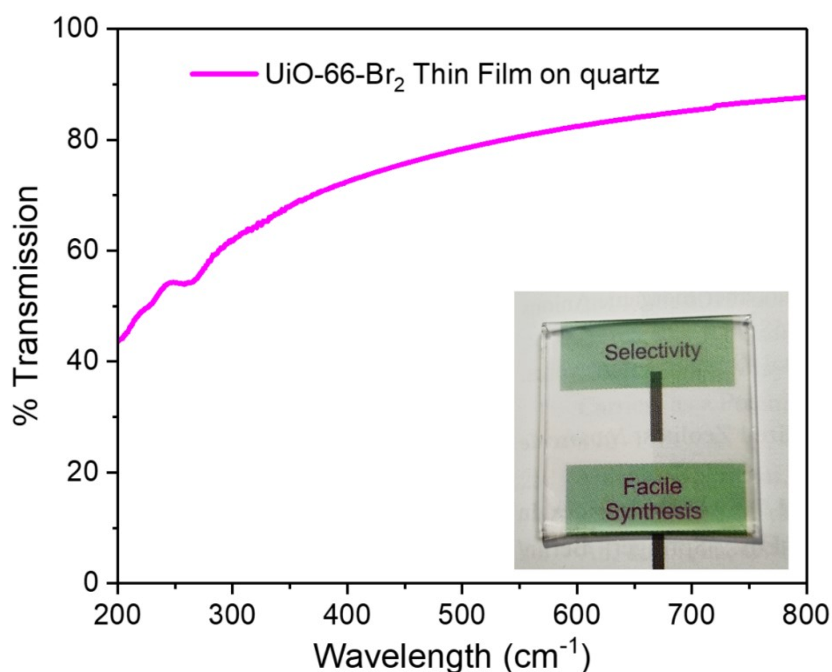

Figure S26. Transmission spectra (at 298 K) of the UiO-66-Br_2 thin film synthesized by the new ambient condition.

Analysis of mass uptake kinetics

We have measured the mass uptake rates of the thin films grown on quartz crystal microbalance (QCM) sensors with MUD functionalized Au-surface. Methanol (kinetic diameter ~ 3.6 Å, under 50 ml/min N_2 flow), water (kinetic diameter ~ 2.65 Å, under 50 ml/min N_2 flow), 1-propanol and 2-propanol (kinetic diameter ~4.7-4.9 Å, under N_2 flow 40 ml/min) was used as probe molecules because these are smaller in kinetic diameter then the pore window size. The QCM sensors coated with thin films were mounted in a fluidic cell in a temperature controlled environment. Then the vapour uptake rates was measured by monitoring the fundamental frequency change over time.

The Sauerbrey equation describes the mass-frequency relationship of a Quartz Crystal Microbalance (QCM) sensor.

$$\Delta m = -c\frac{\Delta f}{n}$$

Here *n* represents the overtone order (specifically *n* = 3, 5, and 7) and *c* stands for the mass sensitivity constant. For a quartz crystal with a frequency of 5 MHz, the value of *c* is 17.7 $ng.cm^{-2}$. We analysed the data under the assumption of Fickian diffusion, which means we considered a constant diffusivity, *D*, that does not change with varying vapour concentrations.

$$\frac{M_f(t)}{M_\infty} = 1 - \frac{8}{\pi^2}\sum_{m=0}^{\infty}\frac{1}{(2m+1)^2}exp(-\frac{4D\pi^2 t(2m+1)^2}{L^2})$$

Here, $M_f(t)$ represents the amount of substance (in nanograms) adsorbed at time t, M stands for the amount adsorbed at the infinite time (i.e. at equilibrium), *D* is expressed in square meters per second and L denotes the thickness of the film.

Diffusivity, *D*, is calculated using the following linear equation: [19]

$$\frac{M_t(t)}{M_\infty} \approx \frac{8}{\sqrt{\pi}}\sqrt{\frac{Dt}{L^2}}$$

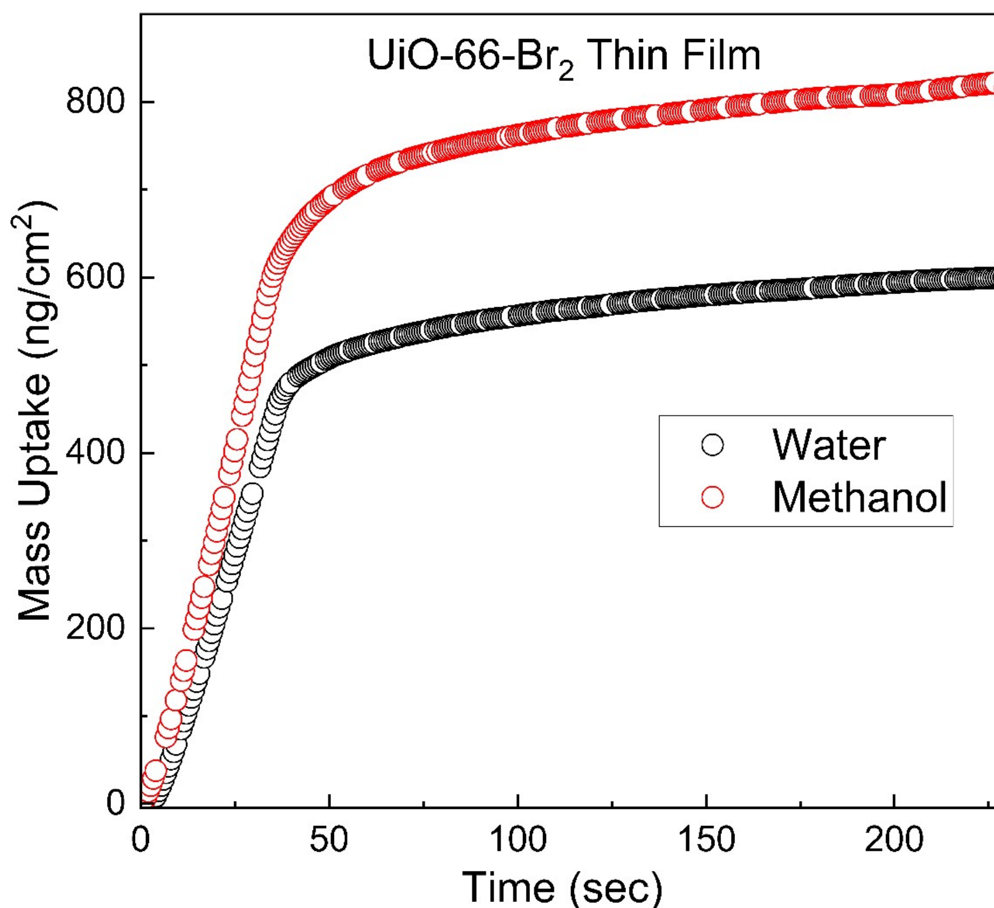

Figure S27. Water and methanol vapour uptake profiles of the UiO-66-Br_2 thin films at 298 K.

1. M. R. DeStefano, T. Islamoglu, S. J. Garibay, J. T. Hupp and O. K. Farha, *Chemistry of Materials*, 2017, **29**, 1357-1361.
2. I. Hod, W. Bury, D. M. Karlin, P. Deria, C.-W. Kung, M. J. Katz, M. So, B. Klahr, D. Jin, Y.-W. Chung, T. W. Odom, O. K. Farha and J. T. Hupp, *Advanced Materials*, 2014, **26**, 6295-6300.
3. M. Miyamoto, S. Kohmura, H. Iwatsuka, Y. Oumi and S. Uemiya, *CrystEngComm*, 2015, **17**, 3422-3425.
4. K. B. Lausund and O. Nilsen, *Nature Communications*, 2016, **7**, 13578.
5. T. Hashem, E. P. Valadez Sánchez, P. G. Weidler, H. Gliemann, M. H. Alkordi and C. Wöll, *ChemistryOpen*, 2020, **9**, 524-527.
6. A. L. Semrau and R. A. Fischer, *Chemistry – A European Journal*, 2021, **27**, 8509-8516.
7. A. Ghorbanpour, L. D. Huelsenbeck, D.-M. Smilgies and G. Giri, *CrystEngComm*, 2018, **20**, 294-300.
8. L. N. Appelhans, L. Hughes, B. McKenzie, M. Rodriguez, J. Griego, J. Briscoe, M. Moorman, E. Frederick and J. B. Wright, *Microporous and Mesoporous Materials*, 2021, **323**, 111133.
9. A. Micero, T. Hashem, H. Gliemann and A. Léon, *Journal*, 2021, **11**.

10. A. L. Semrau, S. Wannapaiboon, S. P. Pujari, P. Vervoorts, B. Albada, H. Zuilhof and R. A. Fischer, *Crystal Growth & Design*, 2019, **19**, 1738-1747.
11. E. Virmani, J. M. Rotter, A. Mähringer, T. von Zons, A. Godt, T. Bein, S. Wuttke and D. D. Medina, *Journal of the American Chemical Society*, 2018, **140**, 4812-4819.
12. Y.-H. Xiao, Z.-G. Gu and J. Zhang, *Science China Chemistry*, 2020, **63**, 1059-1065.
13. I. Stassen, M. Styles, T. Van Assche, N. Campagnol, J. Fransaer, J. Denayer, J.-C. Tan, P. Falcaro, D. De Vos and R. Ameloot, *Chemistry of Materials*, 2015, **27**, 1801-1807.
14. P. K. Verma, L. Huelsenbeck, A. W. Nichols, T. Islamoglu, H. Heinrich, C. W. Machan and G. Giri, *Chemistry of Materials*, 2020, **32**, 10556-10565.
15. S. Jung, P. Verma, S. Robinson, E. Beyer, H. Hall, L. Huelsenbeck, K. H. Stone and G. Giri, *Industrial & Engineering Chemistry Research*, 2021, **60**, 17585-17595.
16. J. Yan, Y. Sun, T. Ji, Y. Liu, N. Zhang, B. Sun, S. Meng, B. H. Yin, M. Wu, H. Hu and Y. Liu, *Industrial & Engineering Chemistry Research*, 2023, **62**, 5973-5983.
17. Y. Sun, J. Yan, Y. Gao, T. Ji, S. Chen, C. Wang, P. Lu, Y. Li and Y. Liu, *Angewandte Chemie International Edition*, 2023, **62**, e202216697.
18. D. Ma, G. Han, Z. F. Gao and S. B. Chen, *ACS Applied Materials & Interfaces*, 2019, **11**, 45290-45300.
19. O. Zybaylo, O. Shekhah, H. Wang, M. Tafipolsky, R. Schmid, D. Johannsmann and C. Wöll, *Physical Chemistry Chemical Physics*, 2010, **12**, 8093-8098.